Defects created in N-doped 4H-SiC by flexion in the brittle regime: Stacking fault multiplicity and dislocation cores.

Maryse Lancin, Michael Texier, Gabrielle Regula, Bernard Pichaud

Defects created in N-doped 4H-SiC by flexion in the brittle regime: Stacking fault multiplicity and dislocation cores.

Journal:	*Philosophical Magazine & Philosophical Magazine Letters*
Manuscript ID:	TPHM-08-Oct-0389.R1
Journal Selection:	Philosophical Magazine
Date Submitted by the Author:	13-Mar-2009
Complete List of Authors:	Lancin, Maryse; CNRS, IM2NP Texier, Michael; Paul Cezanne University, IM2NP Regula, Gabrielle; Paul Cezanne University, IM2NP Pichaud, Bernard; Paul Cezanne University, IM2NP
Keywords:	CTEM, defect structures, dislocations, FIB, HRTEM, microstructure, quantum wells, SiC
Keywords (user supplied):	stacking fault

Defects created in N-doped 4H-SiC in the brittle regime: Stacking fault multiplicity and dislocation cores.

M. LANCIN*[1], M. TEXIER[1], G. REGULA[1], B. PICHAUD[1]

[1] Institut Matériaux Microélectronique Nanosciences de Provence, UMR-CNRS 6242, Université Paul Cézanne, 13397 Marseille-cedex20 –France

Defects are introduced in $[11\bar{2}0]$ N-doped 4H-SiC by surface scratching and bending at 823K or 973K. They are characterized by weak beam-dark field TEM, HRTEM, LACBED, image analysis and dislocation core reconstructions. They consist of double stacking faults (DSFs) dragged by PD pairs in planes in which the Si-C dumbbells have the same orientation. The PDs forming a pair always have the same Burgers vectors. The reconstructions prove that their core composition depends on the dislocation character, the expansion direction and the orientation of the dumbbells in the glide planes. Only Si(g) are mobile, the lack of mobility of C(g) explaining why only three kinds of half-loops expand and why one DSF is always edged by two identical PDs. It is shown that the line morphology is not a sufficient criterion to determine the core composition. Though mechanical stresses are applied, extra thermodynamic and/or electronic driving forces influence the DSF formation in our experiments.

- *Maryse Lancin : **contact author**
Institut Matériaux Microélectronique Nanosciences de Provence, UMR-CNRS 6242,
Université Paul Cézanne, 13397 Marseille-cedex20 –France,
Tel: 00 33 4 91 28 27 56 Fax : 00 33 44 91 28 27 93 e-mail :marsye.lancin@univ-cezanne.fr
- Michaël Texier :
Institut Matériaux Microélectronique Nanosciences de Provence, UMR-CNRS 6242,
Université Paul Cézanne, 13397 Marseille-cedex20 –France,
Tel: 00 33 4 91 28 80 98 Fax : 00 33 44 91 28 27 93 e-mail : michael.texier@univ-cezanne.fr
- Gabrielle Regula :
Institut Matériaux Microélectronique Nanosciences de Provence, UMR-CNRS 6242,
Université Paul Cézanne, 13397 Marseille-cedex20 –France,
Tel: 00 33 4 91 28 80 98 Fax : 00 33 44 91 28 27 93 e-mail : gabrielle.regula@univ-cezanne.fr
- Bernard Pichaud :
Institut Matériaux Microélectronique Nanosciences de Provence, UMR-CNRS 6242,
Université Paul Cézanne, 13397 Marseille-cedex20 –France,
Tel: 00 33 4 91 28 83 11 Fax : 00 33 44 91 28 27 93 e-mail : bernard.pichaud@univ-cezanne.fr

1. Introduction

SiC was first developed for thermo-mechanical applications because of its high strength, its great wear resistance and its low thermal expansion coefficient. The potentialities of this ceramic semiconductor which possesses a large band gap were not ignored but its applications require a drastic control of the polytype homogeneity, doping level and crystalline perfection of materials. The challenge, now overcome, consisted in growing ingots made up of a sole kind of polytype and containing a few micro-pipes, a dislocation density lower than $10^4 cm \times cm^{-3}$ and controlled impurity content. With such single crystals, it is possible to carry out fundamental research in order to correlate the dynamics and structural characteristics of the dislocations. Indeed, the dislocation dynamics is only known thanks to controversial theoretical and experimental results. Many experiments on the more common polytypes -3C, 4H, 6H- give the lowest activation energy for silicon core partial dislocations (PD) [1-6] whereas other studies show similar mobility for both carbon and silicon core PDs [7]. Note that the leading PDs are identified using the same technique (weak beam-dark field (WB-DF) imaging). In addition, first principle calculations give lowest activation energies of migration for the carbon core PDs [8,9]. Another controversial issue has recently focused interest. It concerns the multiplicity of the stacking faults (SFs) created in the brittle regime in highly N-doped 4H-SiC. Indeed, the identified defects consist of single stacking faults (SSFs) [2,4,5], double stacking faults (DSFs) [7] or multiple stacking faults (MSFs) [7, 10]. The observed differences are particularly a matter of concern when the stacking is determined by HRTEM. To account for these discrepancies, different influences of the possible driving forces may be set forth. Three driving forces - thermodynamic, electronic and mechanical - may indeed play a role in these ranges of temperature and doping level ($N = 5\times10^{18} cm^{-3}$ - 9×10^{19} cm^{-3}) but their respective weight may vary depending on the deformation process or the N content. It thus appeared interesting to check the role of these driving forces while using a method which allows characterising unambiguously individual stacking faults and their bounding partial dislocations (PDs). To begin with, this work is carried out in N-doped 4H-SiC ($2 \times10^{18} cm^{-3}$), which is the most promising material for power electronics and hence was commercially available in wafers of high crystalline perfection. The temperature range of the deformation was chosen according to the literature to develop preferentially Shockley PDs leaving SFs in their wakes. Our know-how regarding one deformation procedure suitable for semiconductors such as silicon or gallium arsenide was adapted to silicon carbide. Using this procedure, the nucleation occurs at or next to the surface and the defects expand in a well controlled stress field [11]. The density of created defects being low enough, it was possible to characterize individual stacking faults and their bounding PDs by coupling chemical etching, TEM techniques –WB-DF and HRTEM imaging, - with image contrast analysis and dislocation core reconstructions. In a first study performed at 823 K, we have characterised DSFs dragged by Si(g)

PDs [12, 13]. However, because of the above mentioned discrepancies, we found interesting to perform further investigations paying attention to obtain good statistics on the fault stacking and core composition of the PDs. Moreover, we have included large angle convergent beam electron diffraction (LACBED) to our TEM studies [14] which is a powerful tool to characterise the PD core when coupled with core reconstructions. Besides, we have characterised PDs on each side of the SF intersections with the sample surface and investigated the orientation of the leading PDs versus the applied stress. This paper reports the analysis of all results which allows to discuss the PD mobility versus their core and to understand the features of the DSF expansions.

2. Materials and techniques

N-doped 4H-SiC was purchased from Cree Research™. The N content was controlled by photoluminescence measurements and found to be 2×10^{18} cm^{-3} [15]. The density of dislocations in the basal plane measured by X-Ray-Topography was lower than $10^4 cm.cm^{-3}$ [11].

The 20×5×0.2 mm^3 samples were cut by Cree Research so that their length (X axis) was at 45° from the glide planes. The dislocation sources were obtained by a scratch on the $(11\bar{2}0)$ surface and the defect expansion by annealing under cantilever bending in the brittle regime at 823 K or 973 K [11]. After annealing, the samples were chemically etched and imaged with an optical microscope.

(0001) thin foils for WB-DF TEM and LACBED investigations were prepared by the Focused Ion Beam technique (FIB) at the fault tips. Before ion thinning, platinum was deposited on the sample surface along the fault emergence to avoid any ion erosion. The dislocation lines were imaged by WB-DF TEM with 200 keV microscopes (FEI™ and 200CX Jeol™). The line, direction and modulus of the Burgers vectors were determined by LACBED using a 2010-FEG Jeol™ microscope operating at 197 keV [14]. $(11\bar{2}0)$ thin foils for HRTEM imaging were prepared by back-side mechanical polishing and ion-beam milling to electron transparency. They were cleaned with Ar plasma to remove the contamination introduced by the sample preparation. HRTEM studies were carried out with a 2010-FEG Jeol™ microscope equipped with a GIF and a CCD camera (Gatan™) or a 4000EX Jeol™ microscope equipped with a CCD camera (Gatan™). A few focal series were performed [12] but most of the defects were imaged when the minimum of contrast was obtained on the amorphous layer created by the thinning process. Indeed, such a defocus could unambiguously be selected during the experiments.

The simulation of the image contrast was performed using the multi-slice method implemented with the EMS software [16]. The absorption and Debye–Waller coefficients were equal to 0.04 and 0.004 nm^2 for Si and to 0.03 and 0.004 nm^2 for C, respectively. The selected sample thickness (3nm) provided the

best fit between experimental and simulated contrasts but it is known that this value is much lower than the true one [17].

The respective positions of Si and C atomic columns in the sample were verified by analysis of the $\{11\bar{2}0\}$ image contrast [18] (figure 1). At the minimum of contrast (resp. Scherzer), the projections in a $\{11\bar{2}0\}$ plane of the Si and C atomic columns which are 0.109 nm apart and form the dumbbells could not be resolved on the images and appeared as white (resp. black) dots. However, they could be localized using the respective positions of the dots in the two sets of glide planes labelled G1G2 and G3G4 (quoted ++ and – – respectively in the Hägg notation, with which we think that our results would be less clearly stated). Inside the thick parts of experimental images, G1G2 could be easily distinguished from G3G4 using their "black and white contrast" [19].

3. Results

3.1 Identification of the faults expanding during annealing

The etch patterns obtained on the $(11\bar{2}0)$ face in all the samples annealed at 823 K [12] or at 973 K (figure 2) consist of lines that stretch at 45° from the scratch and thus are parallel to the basal planes. They correspond to the intersections of planar defects with the surface. As previously reported for 823 K [12], three populations of defects labelled A, B and C can be categorised thanks to their propagation direction and their length. The A defects expand as a function of the bending stress in the P1= $[\bar{1}100]$ direction. They are nucleated next to the scratch and also next to the sample border labelled "edge1" in figure 2. Notice that the sample edges were not smoothed after the sample cutting and thus could act as defect sources. The B defects also glide in the P1 direction, from the scratch or from the sample edge 1, but their lengths are almost independent of the bending stress and remain smaller than 200 microns. The C defects develop from the scratch in the P2 direction. Their lengths reach at the most 400 microns and decrease when the bending stress increases. Notice that no defect develops on the $(11\bar{2}0)$ face in the P2 direction from the sample border labelled "edge2".

The atomic structure of the defects was obtained from high resolution images on $[11\bar{2}0]$ oriented thin foils. At both annealing temperatures, we observe the double faulted layers displayed in figure 3. The ABCB stacking typical of 4H-SiC is transformed into either ABCABC or CBACBA, which are characteristic of a cubic structure (3C-SiC). We thus label them a-3C and b-3C. It is noteworthy that all the identified A defects (49) exhibit the a-3C stacking whereas the entire B population (18) and the entire

C ones (34) have the b-3C stacking, whatever the temperature and the dislocation source location (scratch or sample edge). In the literature, such defects consisting of six cubic Si-C bi-layers being called DSFs, A, B and C defects will hereafter be named DSFA, DSFB and DSFC. Moreover, we always observe DSFs but never SSF and only one multiple fault consisting of 10 cubic Si-C bi-layers. Coupling optical micrographs and HRTEM images, we find that the defects typically develop by batches which are distant of a few tens of microns and which consist of two or three DSFs a few tens of nanometres apart.

To fully characterise the atomic structure of the DSFs, we have localised the projections of the Si and C atomic columns in the $(11\bar{2}0)$ images by analysing the image contrast. The simulated contrast of the a-3C structure and the atomic positions are displayed in figure 3. Note that a-3C and b-3C are defined in the $(11\bar{2}0)$ plane. Thus, the a-3C stacking would be exactly the same, whether obtained in $(\bar{2}110)$ or $(1\bar{2}10)$ planes. On the contrary, it would look like the b-3C stacking if it were observed in $(\bar{1}\,\bar{1}20)$, $(2\bar{1}\,\bar{1}0)$ or $(\bar{1}2\bar{1}0)$ planes, due to the $P6_3mc$ structure of 4H-SiC.

3.2 Partial dislocations dragging the faults

The PDs bounding the DSFs were characterised next to the $(11\bar{2}0)$ surface thanks to WB-DF imaging and LACBED analysis. The characterisations were generally performed on the mobile segments which border the defects in their expansion direction, but some were also performed on the immobile segments located near the scratch. Two significant features are shared by the three populations of DSFs. Indeed, the WB-DF images always reveal two SF_S dragged by two PDs called D1 and D2 at an equilibrium distance of about 100 nm (figure 4). The extinction criterion demonstrates that D1 and D2 bounding each DSF always have the same Burgers vector and thereby are repulsive. Beyond these two similitudes, each population of DSFs exhibits its own characteristics, whatever the temperature or the dislocation source location (scratch or sample edge). In the following, the direction, **L,** of the mobile PD is oriented from the $(11\bar{2}0)$ surface towards the neutral plane when the PD glides in the P1 direction, and vice versa when it expands in the P2 direction.

We selected PDs bounding DSFAs, which expanded during the annealing over 300 microns or more, to avoid any confusion with DSFBs. WB-DF imaging performed on 27 PDs always show that both D1 and D2 exhibit a Burgers vector, **b**, equal to $\pm\, a/3[1\,\bar{1}00]$. LACBED analysis of some of them gives the sign of **b** and thus $\mathbf{b} = a/3[1\,\bar{1}00]$. Concerning the mobile PDs, their lines seem to be local stress dependent. For the smallest bending stresses, the PDs are perfectly aligned along two $[1\bar{2}10]$ Peierls valleys (figure

4a) and are thus true 30° Shockley PDs. For the highest stresses, segments aligned along the $[\bar{1}\,\bar{1}\,20]$ Peierls valley, which are 90° segments, can be identified near the $(11\bar{2}0)$ surface (figure 4b). As the stress decreases (with X or with Z), the PD lines tend to curve and to lie closer and closer to the $[1\bar{2}10]$ Peierls valley and to have a stronger and stronger 30° character (figure 4c).

Contrary to PDs dragging the DSFAs, the mobile PD pairs bounding DSFBs exhibit similar morphologies and lines. They are rather straight and their lines remain within 10° close to the $[\bar{1}\,\bar{1}\,20]$ Peierls valley (figure. 4d). By means of WB-DF TEM, we obtain $\mathbf{b} = \pm\, a/3[10\bar{1}0]$ on the 11 PD pairs analysed, all the PDs identified being thus of the 30° type. The true **b** value measured by LACBED is $a/3[10\bar{1}0]$ (figure 5). In a previous work [12], we concluded that **b** was $\pm\, a/3[0\bar{1}10]$. The error was due to an incorrect location of the $(11\bar{2}0)$ surface in the FIB thin foils. The platinum cap always used in this work to protect the surface prevents such an upside down error.

Concerning the mobile PDs bordering the DSFCs, they are generally curved near the sample surface (figure 4e), their angle with the $(11\bar{2}0)$ plane ranging from 60° to 40°. As expected, the PDs tend to align along the $[2\bar{1}\,\bar{1}0]$ Peierls valleys when they go deeper into the material. WB-DF TEM investigations of the 18 PD pairs analysed give $\mathbf{b} = \pm\, a/3[\bar{1}100]$ whereas LACBED analysis of several PD pairs provides the actual $\mathbf{b} = a/3[\bar{1}100]$. Because of this **b** orientation and despite the line variations, we admit that the PDs are mainly of the 30° type.

The characteristics of the PDs were also investigated near the DSF sources. The morphology of the immobile segments is very similar to that of the mobile ones, whatever their line directions or the DSF types. Figure 4f displays their typical features in the case of PD lines bordering a DSFC. In this case, they are almost stretched along the $[1\bar{2}10]$ Peierls valley.

Table 1 summarises the number and characteristics of the PDs identified. When looking back to figure 3, it is clear that the PD pairs driving DSFAs glide on successive G1G2 planes resulting in the a-3C stacking whereas those dragging DSFBs and DSFCs share two successive G3G4 planes giving the b-3C stacking. Note that the two other associations of two adjacent glide planes (G2G3 or G1G4) cannot create a DSF but two layers of 2H-SiC.

3.3 Core composition

Knowing a PD line and character as well as its type of glide plane - G1 (G2) or G3 (G4) - it is then possible to obtain its core by reconstruction. To better discuss the dislocation formation, we find it more

instructive to first consider all possible loops which result in a-3C and b-3C stackings and determine the core composition of the bounding PDs. To draw them, we choose to consider all possible configurations for a PD pair whose line direction is **L**=$[\bar{1}\,\bar{1}20]$ and which glides in the P1 direction either on G1(G2) or G3(G4) planes (figure 6). The boundaries are rebuilt in the $(11\bar{2}0)$ plane perpendicular to the line in order to obtain the structural units of 90° or 30° PDs, characteristic of elementary semiconductors [20, 21] and observed in 3C-SiC [22]. Obviously, the reconstructions show that the PD core depends on its character (30° or 90°) but also on its glide plane and thus is related to the a-3C or b-3C stacking. As an example, 90° PD pairs have a silicon core and result in the a-3C stacking when they glide on G1G2 whereas they have a carbon core and induce the b-3C stacking when they drive the fault on G3G4. Note that the upper reconstruction in figure 6a corresponds to the 90° PD pairs dragging some DSFAs and the lower one in figure 6b, to the 30° PD pairs leading the DSFBs.

The possible Burgers vectors of the different PDs may be determined by drawing the Burgers circuit and using the starting finish/right hand convention. For the 90° PD, we found the **b** modulus and sign since the vector is in the $(11\bar{2}0)$ plane and, indeed, the **b** = a/3$[1\,\bar{1}00]$ determined for DSFA is in perfect agreement with the result obtained separately by LACBED. In the case of 30° PDs however, two possible Burgers vectors correspond to the same reconstruction because it is actually the projection of **b** in the $(11\bar{2}0)$ plane which is determined. By coupling the results with those obtained by WB-DF TEM, it is possible to deduce the modulus and sign of **b**. As an example, lets us consider a PD pair leading a DSFB. The reconstruction results in **b**= a/3$[0\,\bar{1}10]$ or **b** = a/3$[10\bar{1}0]$ whereas WB-DF analysis gives b = ± a/3$[10\bar{1}0]$, hence the actual **b** must be a/3$[10\bar{1}0]$. Of course, we found the **b** modulus and sign of DSFBs measured by LACBED.

Based on the reconstructions, all the possible loops which result in the a-3C or b-3C stacking can be sketched (figure 7). As it is well known, in such theoretical loops, the partial segments follow the Peierls valleys. In a compound semiconductor such as SiC, only six loops may expand in the material. Moreover, because the PD sources are located on or very near the $(11\bar{2}0)$ surface, only half loops could develop during the deformation process. One DSF consists of two half loops expanding in successive G1G2 or G3G4 glide planes. In figure 7, the three observed populations of DSFs are indicated.

We think important to underline here the potentialities of the method used to characterise the defects. The reconstructions allow the PD core determination, knowing the stacking and the propagation direction of the fault as well as the PD characteristics obtained by WB-DF TEM (line and Burgers vector direction). In addition, and very interestingly, these reconstructions give the PD core and the stacking of the fault when the PD Burgers vector modulus and sign are determined by LACBED. Figure 7 shows that a PD pair

whose line direction is **L** = $[\bar{1}\,\bar{1}\,20]$ and whose **b** is equal to a/3$[10\bar{1}0]$ has a Si-core and necessarily glides in G3G4 inducing the b-3C stacking observed separately by HRTEM for DSFBs. Hence, core reconstructions make it possible to match HRTEM and LACBED without any ambiguity.

4. Discussion

The deformation procedure selected induces the nucleation of PD pairs, gliding on adjacent glide planes in which the Si-C dumbbells have the same orientations, resulting in the formation of DSFs, whatever the temperature, the source location or the applied stress. Surprisingly, it promotes half loop glide on only one side of the scratch, either in the P1 or P2 direction. Moreover, it creates only three of the six populations expected according to the reconstructions (figure 7). It is noteworthy that all the identified PDs dragging the DSFs have a silicon core. Most of the mobile PDs are of the 30° type but, interestingly, we found some DSFAs driven by Si(g) segments with a 90° character.

To understand such a deformation process, let us first consider the Peach-Koehler force **F** applied on each half-loop by cantilever bending during our experiments [11]. We remind that

$$\mathbf{F} = [\sigma_r]\,\mathbf{b} \wedge \mathbf{L} \qquad (1)$$

and that the resolved shear stress is given by:

$$\sigma_r = \begin{pmatrix} -k & 0 & 0 \\ 0 & 0 & 0 \\ 0 & 0 & 0 \end{pmatrix} \qquad (2)$$

with k(X,Z) being positive above the neutral plane (zone under compression); k depends on the SiC Young modulus (E), the sample thickness (e), the Schmid factor (s) and the curvature radius R(X). Therefore, three of the possible half-loops (HL1, HL5 and HL6) expand under a compressive stress and the other three (HL2, HL3 and HL4) under a tensile one. With the $(11\bar{2}0)$ face submitted to a compressive stress, we would expect symmetric expansions of HL1, HL5 and HL6 but we only observe an asymmetric glide of the HL1 pairs (DSFAs), HL6 pairs (DSFBs) and no HL5. This implies that the Si(g) segments are much more mobile than the C(g) ones. Under such a condition, a loop containing only one Si(g) segment such as HL5 would hardly grow and cannot be detected. The existence of HL4 pairs (DSFCs), which are not expected on this face and which never extend from the sample edge 2, proves that the deformation induced by the scratch provides a glide force expanding them in the P2 direction; this is similar to what a tensile stress would do. This force however, has limited impact as compared to a compressive stress. Actually, the expansion of DSFCs is very little and decreases as this compressive stress increases. The

asymmetry of HL4 propagation also confirms the different mobility of the PDs as a function of their core compositions.

At this point, a question arises: when a DSF is created, why ~~it~~ is it always dragged by a pair of identical partials? Despite the complexity of the stress field next to the scratch, it is clear that two PDs nucleated on two adjacent glide planes must relieve either compressive or tensile stress. Let us consider the PDs which glide in the P1 direction to relieve a compressive stress. We have seen that PD pairs must glide either in G1G2 or in G3G4 to form a DSF. In G1(G2), only HL1 expands under compressive stress and thus two identical loops must be created. In G3(G4), if HL5 is created, its expansion is blocked by its immobile C(g) segments, as already mentioned, and, hence, the only possibility to obtain a DSF is to nucleate two HL6. The existence of only identical PDs in a pair is perfectly consistent with the greater mobility of Si(g) as compared to C(g). The lack of mobility of C(g) also prevents the expansion of fronts of two PDs - as observed in 3C-SiC at higher temperatures [22] - which would also result in DSFs without the contradictory effect of the repulsion of dislocations with identical Burgers vectors. Indeed, such fronts would consist of a combination of 90°Si(g) and 30°C(g) or vice versa.

The mobility of Si(g) and C(g) were reported in heavily N-doped (~ 10^{18}-. 10^{19}cm^{-3}) 4H-SiC. They were obtained for similar temperatures and applied stresses than those we used but thanks to different deformation procedures. During compression and indentation tests [5, 2], the faulted loops which might expand to relieve the stresses were always dragged by Si(g). However, both Si(g) or C(g) were identified during compression under confining pressure [7]. Moreover, at a higher temperature (1423 K), near the brittle-ductile transition, Chung et al. [23] reported the expansion of DSFs dragged by Shockley PDs in N-doped (9×10^{19}cm^{-3}) 4H-SiC after surface damaging and annealing. By reconstruction of the cores of the PDs displayed in figures 2 and 3 of ref [23], we found that the DSFs are necessarily driven by 30°PDs with different core compositions, namely 30°Si(g) and 30°C(g). In view of these discrepancies, the role of the dislocation nucleation appears to be a relevant parameter.

In our samples, almost all the Si(g) identified near the sample surface are of the 30° type. However, results obtained on the DSFAs prove that the deformation process provides enough energy to create 90°Si(g). The mobility of the Si(g) as a function of their character and of the bending stress will be fully discussed elsewhere [24].

During the deformation, C(g) segments can be created, even if they hardly move. Indeed, as an example, we have shown in figure 4f that the immobile PD segment bounding one DSFC is almost parallel to the $[1\bar{2}10]$ Peierls valley and thus consists of 30° C(g) (cf. left part of HL4 in figure 7). Moreover, the DSFB expansion only observed in the P1 direction implies that the 30°C(g) segment of HL6 is created and blocks the glide in the P2 direction. Our work is thus in perfect agreement with that of Pirouz et al., as far as the character and core composition of the mobile PDs are concerned.

Concerning the C(g) morphology however, there is some discrepancy between our work and what is generally admitted. Let us again consider the C(g) segments observed near the sample surface (line $[1\bar{2}10]$ in figure 4f). Though they look more rugged than the Si ones - since they do have a few pinning points - they do not exhibit the marked ziz-zag morphology very characteristic of the C-core PDs created by indentation in 4H-SiC [2] and in 3C-SiC [1] by Pirouz et al. or observed in PiN diode by Twigg et al.[25]. In their deformed samples, Mussi et al [7] found C(g) core PDs with either a straight or a zigzagged-line. Mussi's and our results show that the line morphology of a PD is not a sufficient criterion to deduce its core composition.

Now let us compare our results with the predictions of the theoretical computations performed in SiC. Blumeneau et al [8] showed that the core energy of the PDs is almost independent of the polytype and that their calculations performed on 3C and 2H polytypes can apply to 4H-SiC. They obtained a core energies smaller for the Si(g) than the C(g) and lower for the 30° Si(g) than the 90°Si(g). They also found that the C(g) are more mobile than the Si(g), the 90°C(g) being the quickest. Savini et al. calculated the migration energies of PDs [9]. They used asymmetric core reconstructions, as Blumeneau et al. did, as well as symmetric ones (SR). The latter were the most mobile and were found to be the most stable in heavily N-doped materials, consistent with our experiments. The activation energy of migration was found to be the smallest for the SR 90° C(g) (0.61 eV) and almost the same for the SR 30°C(g) and the SR 90°Si(g) (1.57 eV and 1.55 eV, respectively). In our experiments, the possible highest formation energy of C(g) did not prevent their formation. However, because the 30°C(g) can be nucleated by our deformation, if they were as mobile as the 90°Si(g) or quicker, we would have observed symmetric expansions of the half loops on each side of the scratch, instead of the asymmetric ones observed. Hence, there are still large discrepancies between experiments and calculations. However, as suggested by Blumenau et al. [8], these discrepancies may originate in the N content of the samples used in the above mentioned experiments. Indeed, the nitrogen atoms which are always located on the carbon sites may create a barrier to kink migration along the C-core partial dislocations and thus decrease their mobility. Velocity measurements in intrinsic 4H-SiC would be useful to verify this assumption.

The variations in the PD mobility as a function of their core compositions explain the asymmetric expansion of the DSFs but not all the deformation features. The different expansions of DSFAs and DSFBs are a consequence of the compressive force due to bending which is, for a given stress, two times greater on DSFA than on DSFB. Though both DSFAs and DSFBs are nucleated by the scratch or the sample-cutting damage, the primary glide system involving DSFAs is the first to be activated by bending and DSFAs are driven far from their origin. Their expansions must be sufficient to relieve the bending stress and to prevent or limit the activation of the secondary glide system which involves the DSFBs.

The most intriguing feature of our deformation experiments is the creation of DSFs dragged by two repulsive PDs. The mechanism proposed for multiple SF formation [10] cannot explain the systematic creation of DSFs. If the stress fields were sufficient to promote one dislocation cross slip, there would not be any reason to limit this process to one single event. A second or several others should be promoted leading to MSFs, in particular for higher resolved shear stresses.

The systematic formation of DSFs and the presence of close repulsive PDs imply that extra driving forces, other than mechanical ones, should play a determinant role in our deformation process. These forces must provide the energy necessary to create and expand the faults in the 4H structure and to counterbalance the repulsive forces between the PDs. The energy costs to form stacking faults of various thicknesses have been evaluated by Iwata et al. in pure 4H-SiC [26, 27]. They have calculated the stacking fault energy γ_{sf} to create one SF and a second SF next to the first one, in order to form a DSF. They found 17.4mJ/m^2 for the former and 4.7mJ/m^2 for the latter. Moreover, γ_{sf} of the third and fourth neighbouring faults which would increase the cubic layer thickness are equal to 20.3mJ/m^2 and 5.4mJ/m^2, respectively. According to these calculations, the energy cost of a DSF is similar to that of a SSF and lower than the one necessary to create two SSFs. Hence, DSFs should be easily created in pure 4H-SiC but multiple faults should not.

In the literature, two driving forces have been proposed for providing the necessary energy to induce DSF formation and expansion. In one model, the 4H→3C phase transformation provides the energy of formation and glide of PDs, hence expanding the corresponding trailed cubic layer. We suggested this thermodynamic force as a possible extra driving force in our experiments [12, 28] because it is known that N-doping stabilizes the 3C structure [29-31], particularly in the temperature range on consideration. However, if N-doping stabilizes the 3C structure, one would expect a negative γ_{sf} in N-doped 4H-SiC and thus the formation of large cubic layers of various thicknesses, as long as nucleation sites for PDs are available. Numerous nucleation sites are certainly created by our deformation procedure, but we observe only one multiple fault out of 157 defects identified, which involves the glide of two PD pairs in two neighbouring G3G4 glide plane pairs. Hence, the thermodynamic force cannot be the only cause of DSF formation in our experiments.

The most popular model to account for SSFs and DSFs is the quantum well action (QWA). This is linked to energy levels in the band gap due to the faults, which are deeper for DSFs than SSFs. This model was first proposed by Miao et al. to explain SSF expansion in PiN diodes [32]. Using first principle calculations, they showed that a SSF induces energy levels in the band gap. In N-doped material, for suitable temperatures, the lowest level is below the Fermi level and the energy gain per electron trapped at one SF provides the driving force to extend it. Skowronski and co-workers proposed the QWA to explain DSF expansion in N-doped 4H-SiC annealed at 1423K with or without surface grinding [23,33]. The

QWA was also verified by Pirouz et al who observed DSF formation in N-doped wafers [34]. The QWA is a good candidate to explain DSF formation in our samples because in 4H-SiC, for a doping concentration of $N= 2\times10^{18}$ cm^{-3} and a temperature of 823 K or 973 K, the Fermi level is above the lowest energy level of the DSF. In a recent paper, Lambrecht and Miao interpreted the gain in energy to expand a faulted unit area as a driving force applied on the PD(s) bounding the fault [35]. They found this force to be about 100 MPa for a SSF and 850 MPa for a DSF. The latter stress is far larger than the resolved shear stress in our experiments. According to these calculations, SSFs as well as DSFs could form and expand in our materials. As stated above, the nucleation sites are numerous enough in our samples to allow the nucleation of two PDs in two successive glide planes of the same type and thus the expansion of DSFs which reduces the crystal energy more efficiently than SSFs.

5. Conclusion

This paper deals with characterisation of defects which were introduced in N-doped 4H-SiC to study the PD mobility. We develop a powerful approach to individually characterise the stacking faults and the core composition of their bounding PDs. The approach consists in coupling WB-DF imaging and LACBED performed on thin foils milled by FIB at the fault tips, together with HR imaging of the stacking faults, image contrast analysis and core reconstructions.

Core reconstruction of the PDs dragging the six possible faulted-half loops in a compound semiconductor demonstrates that the stacking of the faults and the PD core composition are linked and depend on the dislocation character but also on the glide plane and direction. Only three kinds of faulted-half loops are identified in the samples after surface scratching and annealing under a bending stress. These half loops only expand in one direction, on one side of the scratch. Moreover, they always glide in pairs on planes of identical crystalline structures (i.e., the same Si=C dumbbell orientation) and form six Si-C cubic bi-layers called DSFs. In the three populations of DSFs identified, each defect is dragged by a Si-core PD pair, the Burgers vectors being the same for a given pair. All these structural characteristics imply that C-core PDs can be created but are immobile at the temperatures and stresses under consideration, (823 K-973 K and 0-100 MPa, respectively). The DSF formation also proves that extra thermodynamic and electronic driving forces play a role in N-doped SiC submitted to our deformation procedure.

Acknowledgments

They authors cheerfully thank Dr. J Douin who performed the first WB-DF characterisations and H. Idrissi who performed the sample deformation. The authors greatly thank the "Centre Pluridisciplinaire de Microscopie et de Microanalyse de l'Université Paul Cézanne" where the FEI FIB, 200 keV FEI and 200 keV Jeol 2010F microscopes are available. They gratefully thank Pascale Bayle for allowing access to the Jeol 4000 EX microscope as well as the ONERA-Chatillon and the LPM Poitiers where they performed many WB studies on 200CX keV Jeol microscopes.

References

[1] XJ Ning and P. Pirouz, J. Mat. Res. 11(4) (1996) p. 884.

[2] X.J. Ning, N. Huvey and P. Pirouz, J.Am.Ceram.Soc. 80 (1997) p.1645.

[3] A.V. Samant, W.L. Zhou and P. Pirouz, Phys. Stat. Sol.(a) 166 (1998) p.155.

[4] J.L. Demenet, M.H. Hong and P. Pirouz, Mat. Sci. Forum, 338-342 (2000) p.517.

[5] A.V. Samant, M.H. Hong and P. Pirouz, Phys.Stat.Sol. (b) 222 (2000) p.75.

[6] P. Pirouz, J.L. Demenet and M.H. Hong, Phil. Mag.A 81 (2001) p.1207.

[7] 8a: A. Mussi, J. Rabier, L. Thilly and J.L. Demenet, Phys. stat. sol (c) 4 (20007) p.2929; 7b) private communication.

[8] A.T. Blumeneau, C.J. Fall, R. Jones, S. Öberg, T. Frauenheim and P.R. Bridon, Phys. Rev. B 68 (2003) p.174108.

[9] G. Savini, M.I. Heggie and S. Öberg, Faraday Discuss. 134 (2007) p.353.

[10] P. Pirouz and J.W. Yang, Ultramicroscopy, 51 (1993) p.189.

[11] H. Idrissi, B. Pichaud, G. Regula and M. Lancin, J.Appl.Phys.101 (2007) p.113533.

[12] G. Regula, M. Lancin, H. Idrissi, B. Pichaud and J. Douin, Phil. Mag. Lett. 85 (2005) p.259.

[13] P. Pirouz, M. Zhang, H. McD. Hobgood, M. Lancin, J. Douin and B. Pichaud, Phil. Mag., 86(29-31) (2006) p.4685.

[14] M. Texier, G. Regula, M. Lancin and B. Pichaud, Phil. Mag. Letters 86(9) (2006) p.529.

[15] S. Juillaguet, GES, Faculté des Sciences, Montpellier, private communication.

[16] P. Stadelman, Ultramicroscopy, 21 (1987) p.131.

[17] C.B. Boothroyd, Ultramicroscopy, 83 (2000) p.159.

[18] C. Ragaru, M. Lancin and G. Godon, Eur.Phys. J. Applied Phys 5 (1999) p.135.

[19] Kaiser U, Chuvilin A, Richter W. Ultramicroscopy 1999;76:21.

[20] S. Marklung, Phys. Stat. Sol.(b*),* 92 (1979) p.83.

[21] A. Bourret, J. Thibault-Desseaux and F. Lançon, J. Phys. Paris C4 9 (1983) p.17.

[22] M. Lancin, C. Ragaru and C. Godon, Phil. Mag., B 81 (2001) p.1633.

[23] H. J. Chung, J. Q. Liu, and M. Skowronski, App. Phys. Lett. 81 (2002) p.3759.

[24] J.P. Ayoub, M. Texier, G. Regula, M. Lancin and B. Pichaud, to be published

[25] M.E. Twigg, R.E. Stahlbush, M. Fatemi, S.D. Arthur, J.B. Fedison, J.B. Tucker and S. Wang, Mat. Sci.Forum 457-460 (2004) p.537.

[26] H.P. Iwata, U. Lindefelt, S. Öberg and P.R. Briddon, J. Applied Physics 94 (2003) p.4972.

[27] U. Lindefelt, H. Iwata, S. Öberg and P.R. Briddon, Phys. Rev. B 67 (2003) p.155204.

[28] H. Idrissi, M.Lancin, J. Douin, G. Regula, B. Pichaud, R. El Bouayadi and J.M. Roussel, Mat. Res. Soc. Symp. Proc. 815 (2004) p.J7.2.1.

[29] W.F. Knippenberg, *Philips Res. Reports*, Research Lab. N.V. Philips, Eindhoven, 1963.

[30] K.L.More, J. Ryu, C.H. Carter, J. Bentley and Davis R.F., Advances in Ceramics 23 (1987) p.477.

[31] N.W. Jepps and T.F. Page, Am. Ceram. Soc., (1981) p.C-177.

[32] M. S. Miao, S. Limpijumnong and W.R.L. Lambrecht, App. Phys. Lett. 79 (2001) p.4360.

[33] J. Q. Liu, H. J. Chung, T. Kuhr, Q. Li and M. Skowronski, App. Phys. Lett. 80 (2002) p.2111.

[34] M. Zhang, H.M. Hobgood, M. Treu and P. Pirouz, Mat. Forum. 457-460 (2004) p.759.

[35] W.R.L. Lambrecht, and M.S. Miao, Phys.rev. B 73 (2006) p.155312.

Defects	**DSFA**	**DSFB**	**DSFC**
Expansion direction	P1	P1	P2
Stacking	a-3C	b-3C	b-3C
PD characteristics	**b** = a/3 $[1\bar{1}00]$ **L** = $[1\bar{2}10]$	**b** = a/3 $[10\bar{1}0]$ **L** = $[\bar{1}\bar{1}20]$	**b** = a/3 $[\bar{1}100]$ **L** =~ $[2\bar{1}\bar{1}0]$
Character	30° Si(g)	30° Si(g)	30° Si(g)
Number analyzed	76	29	52

Table 1: Structural characteristics of the DSFs and of their bounding PDs.

We give the PD line orientation and the PD character that are the most characteristic of each of the three populations of DSFs (the possible line variations are detailed in the text).

Figure captions

Figure 1: Stacking of the projections of Si and C atomic columns in HRTEM images of 4H-SiC viewed along a <11-20> axis. The image contrast is simulated using the multislice method (V = 200 kV; Cs = 0.5 nm; defocus spread = 5 nm, semiconvergence angle = 1 mrad, objective aperture = 16 nm^{-1}, slice thickness = 3.1 nm, defocus = 15 nm). The projections of Si (large dots) and C (small dots) atomic columns are superimposed on the simulated images by the software [16]. At the defocus selected, the Si=C dumbbells (Si and C atomic columns 0.109 nm apart) are white. Moreover, the dots reveal the projections of the glide planes belonging to the glide set labelled G1 to G4. Note i) the swap locations of the $(000\bar{1})_{Si}$ and $(000\bar{1})_{C}$ in a) and b) respectively ii) the respective positions of the white dots when the dumbbell orientation changes iii) the link between the dot positions and the locations of Si and C in the dumbbells (see the ellipses) and iv) the dumbbell orientations in G1 and G2 on one hand and in G3 and G4 on the other hand.

Figure 2: **Planar defects revealed by chemical etching and optical microscopy on the $(11\bar{2}0)$surface.** Sample scratched on its $(11\bar{2}0)$surface, annealed under cantilever bending at 973 K and chemically etched with molten KOH for 10 minutes at 773 K: a) the lines parallel to P1= $[\bar{1}100]$ reveal the emergences of planar defects on the $(11\bar{2}0)$ face; b) magnification of the etched patterns near the scratch showing three populations of defects, A, B and C, which can be distinguished thanks to their lengths and their propagation directions P1 or P2 = $[1\bar{1}00]$. The compressive stress increases with X and decreases with Z from σ(X, Z) on the surface to zero on the neutral plane [11].

Figure 3: $[11\bar{2}0]$ **experimental HRTEM images of the 4H structure and of the two kinds of faulted stacking created by the deformation procedure at 823 K or 973 K.**

The white dots correspond to the projections in the image plane of the Si=C dumbbells. The image contrast (left) is simulated using the multislice method (V = 400 kV; Cs = 1 nm; defocus = 8 nm, slice thickness = 3.1 nm, defocus spread = 5 nm, semiconvergence angle = 1 mrad, objective aperture=16 nm^{-1}). The projections of Si (large dots) and C (small dots) atomic columns superimposed to the a-3C stacking are deduced from the image contrast analysis. They are located by the software [16] on the simulated image. For sake of clarity, only the Si stacking sequences are indicated on the drawing. The projections of the glide planes, labelled G1 to G4, are shown.

Figure 4: Lines of the partial dislocations edging DSFs imaged by weak beam dark field near the (0001) axis.

The PD lines are imaged in FIB foils prepared at the dislocation intersections with the surface. 4a to 4c display the typical line orientations of mobile PDs bounding DSFAs which glide either under low (~ 10 MPa), high (~ 80 MPa) or intermediate stress values, respectively. 4d shows the mobile PDs of a DSFB and 4e those of a DSFC. 4f) displays the morphology of immobile PDs edging a DSFC near its source.

Figure 5: Experimental LACBED pattern of a partial dislocation pair bounding a DSFB (left) and the schematic representation of the Bragg line splitting produced by the dislocations and stacking fault (right).

The Burgers vector of the two PDs was determined by indexing the Bragg lines and analysing the splitting using the $\boldsymbol{g.b} = m$ rule [14]. The dashed arrow indicates the position of the PD pair.

Figure 6: Core reconstructions in the $(11\bar{2}0)$ plane perpendicular to the lines of partial dislocation pairs gliding in the P1=$[\bar{1}100]$ direction.

In the drawing, the large and small circles correspond to the projections of Si and C atomic columns respectively. The reconstruction is performed for PD pairs, with **L**=$[\bar{1}\,\bar{1}20]$, gliding either in G1G2 (a) or G3G4 (b) in order to obtain the structural units (coloured) characteristic of 90° or 30° PDs. The core of the 90° PD is determined by the anti-site bond parallel to $[\bar{1}100]$ and that of the 30° PD by the column of atoms which is parallel to $[\bar{1}\,\bar{1}20]$ and links the three faulted circles. The Burgers circuit is drawn and **b** determined using the starting finish/right hand convention. Arrows display the projections in $(11\bar{2}0)$ of the glide planes of the D1 and D2 partials.

Figure 7: Possible faulted half loops created by the glide of partial dislocations in G1 (G2) or in G3 (G4) planes.

Theoretical half loops, whose segments follow the Peierls valleys, which could expand from a scratch performed on the $(11\bar{2}0)$ surface. Under a compressive stress, half loops HL1, HL5 and HL6 would expand and half loops HL2, HL3 and HL4 would shrink. Inside each half loop, the arrow shows the corresponding **b**. The half loop sketches corresponding to DSFA, DSFB and DSFC are indicated.

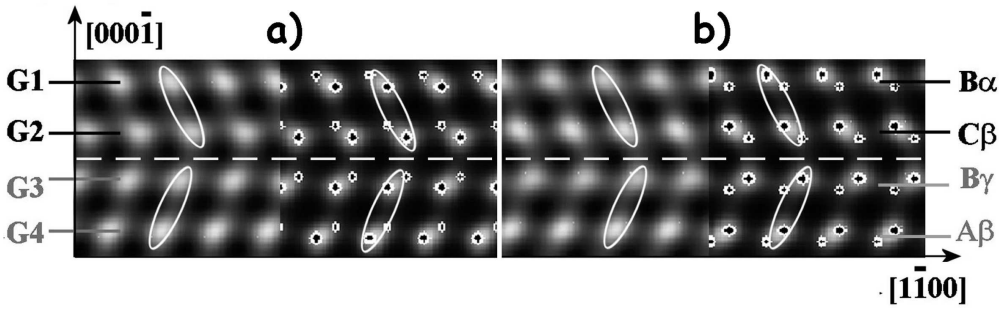

Figure 1
99x30mm (600 x 600 DPI)

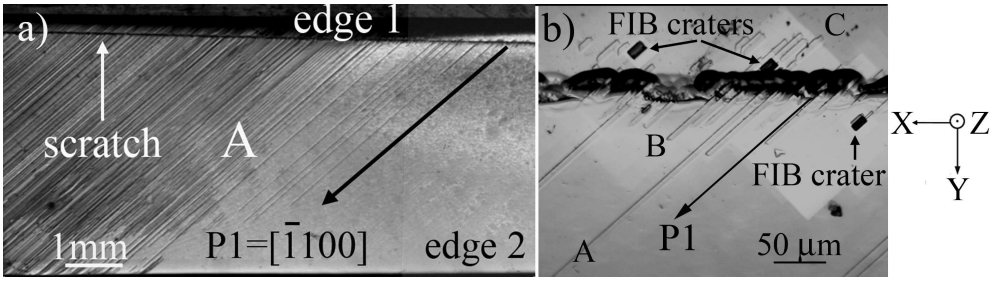

Figure 2
120x32mm (600 x 600 DPI)

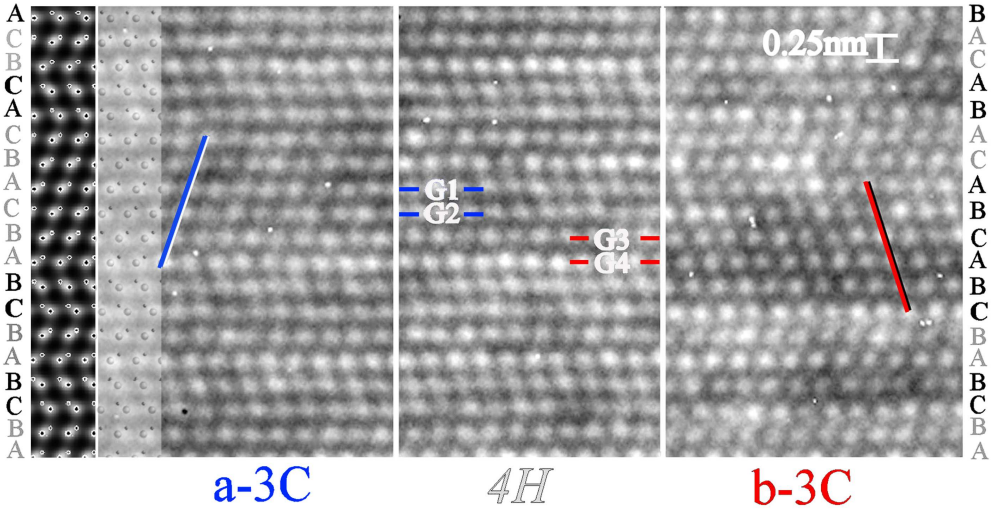

Lancin figure 3
120x61mm (600 x 600 DPI)

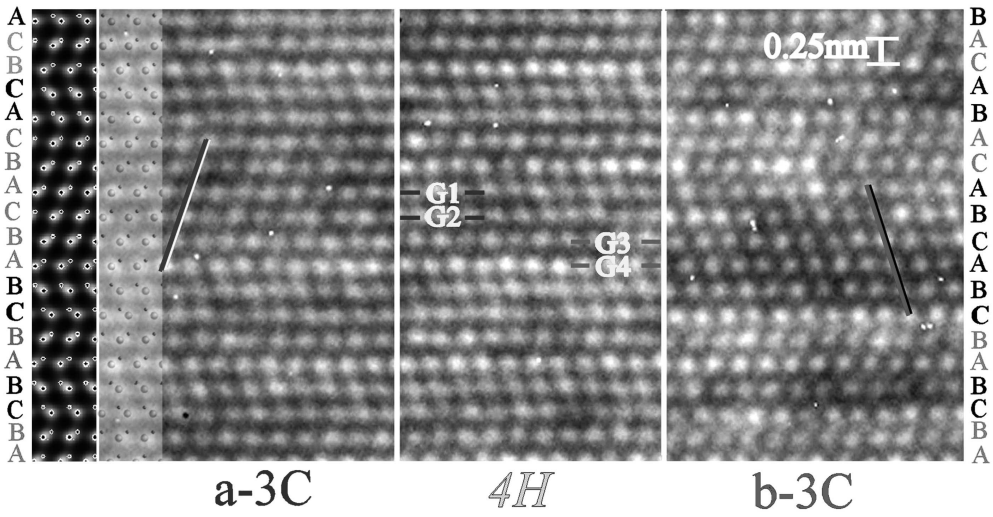

Lancin figure 3 gray
120x61mm (600 x 600 DPI)

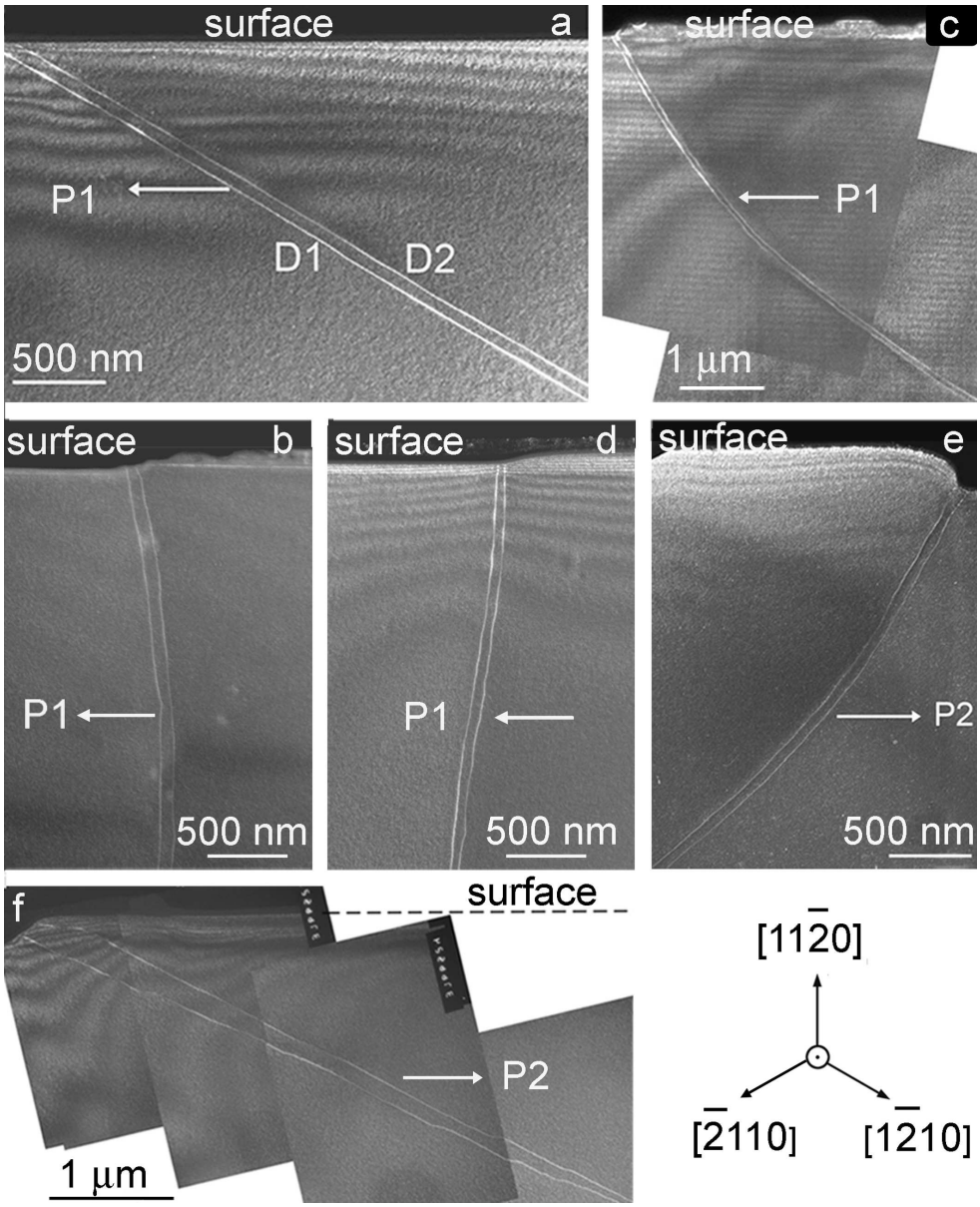

Figure 4
89x109mm (600 x 600 DPI)

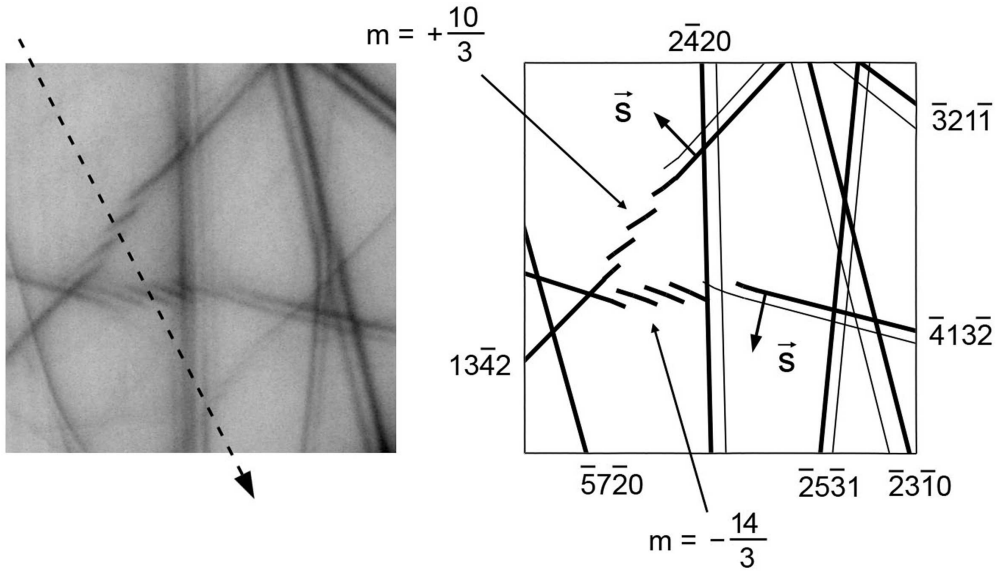

Figure 5
99x57mm (600 x 600 DPI)

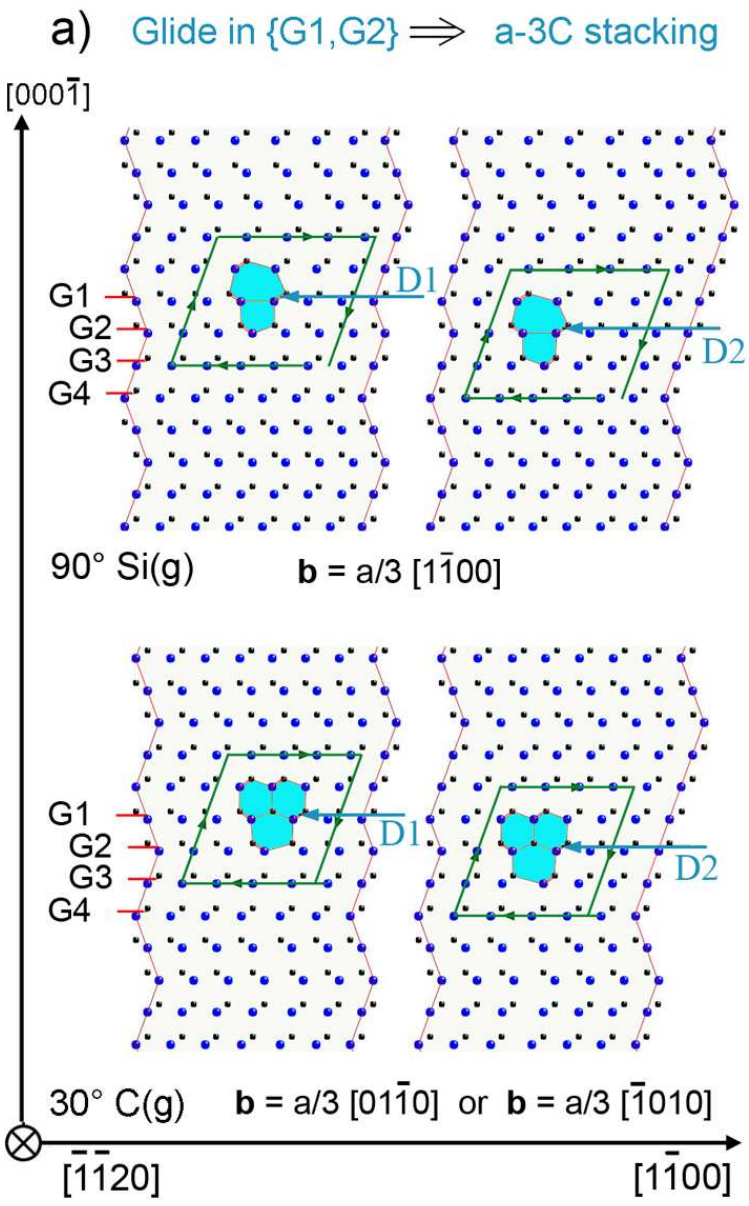

Figure 6a
60x96mm (300 x 300 DPI)

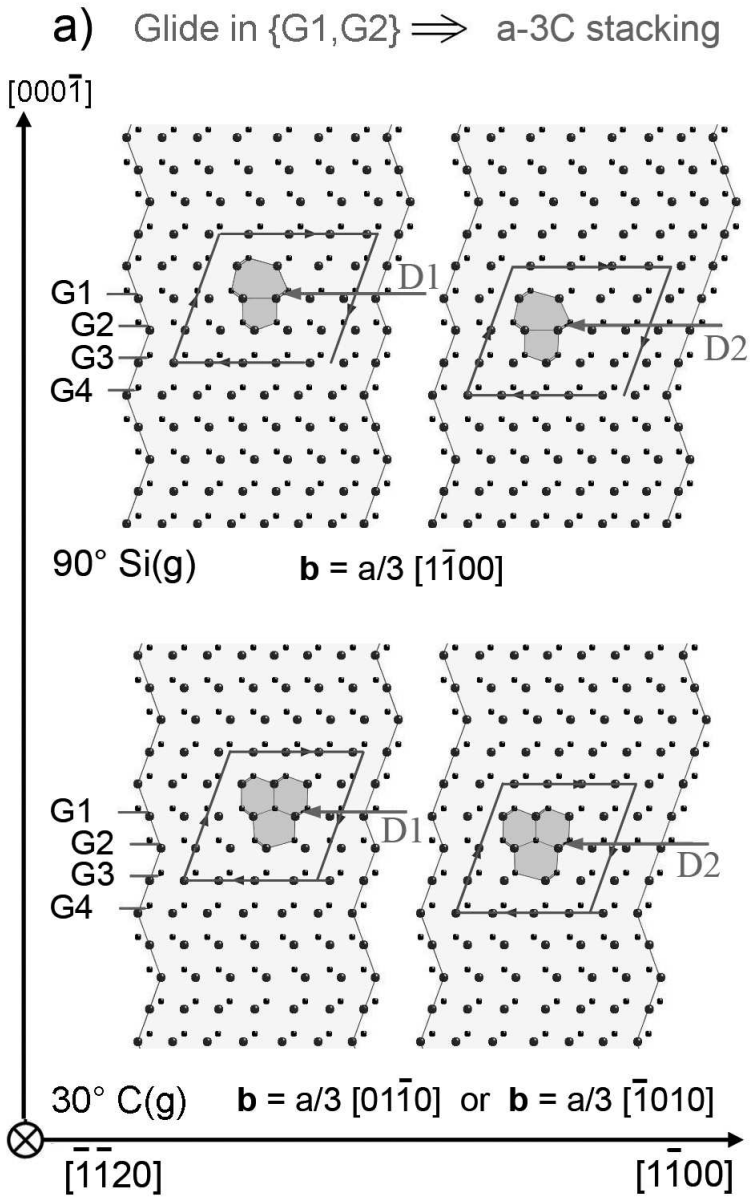

Lancin figure 6a grey
78x126mm (300 x 300 DPI)

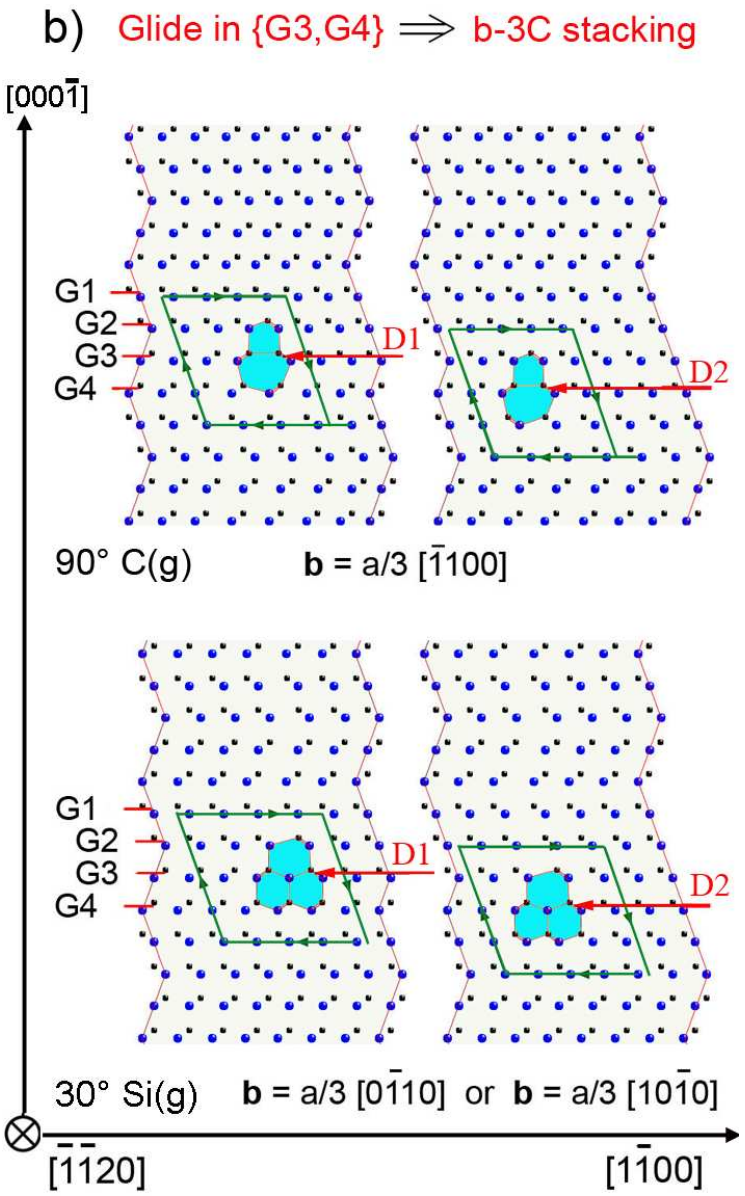

Figure 6b
60x97mm (300 x 300 DPI)

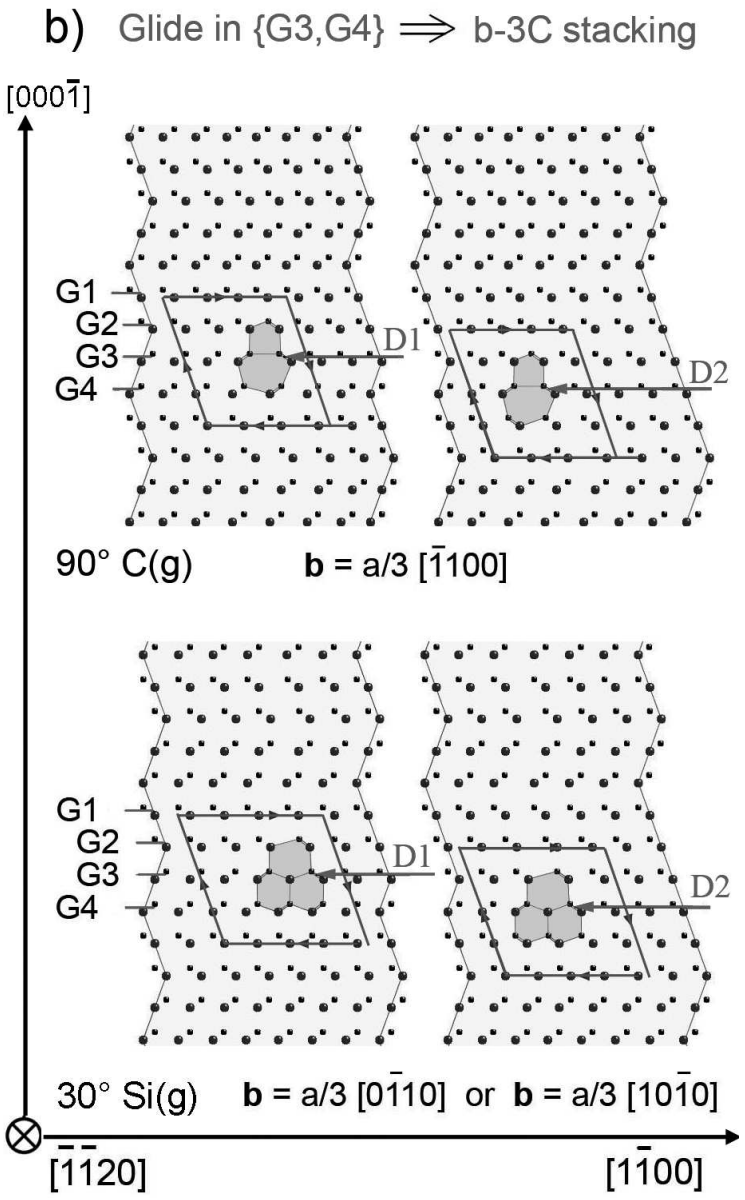

Lancin figure 6b grey
78x127mm (300 x 300 DPI)

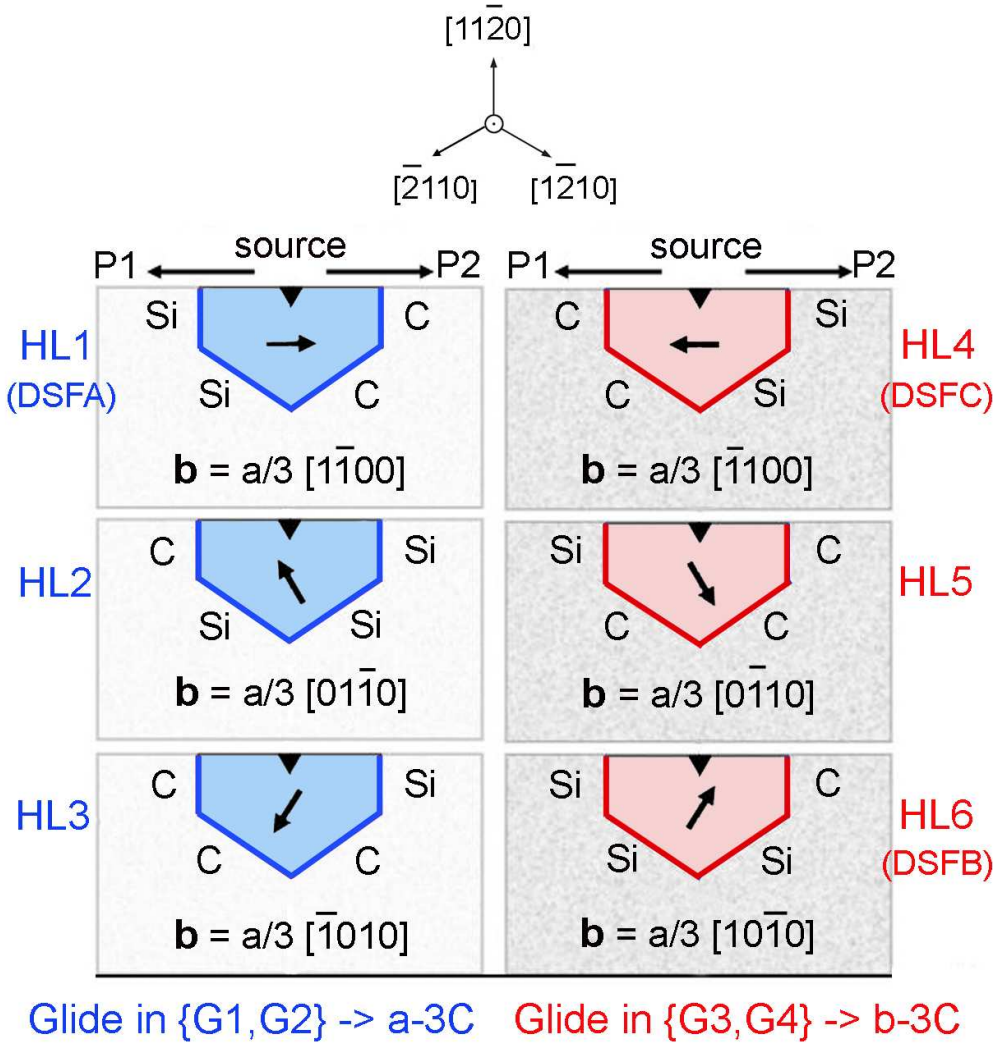

Figure 7
103x110mm (300 x 300 DPI)

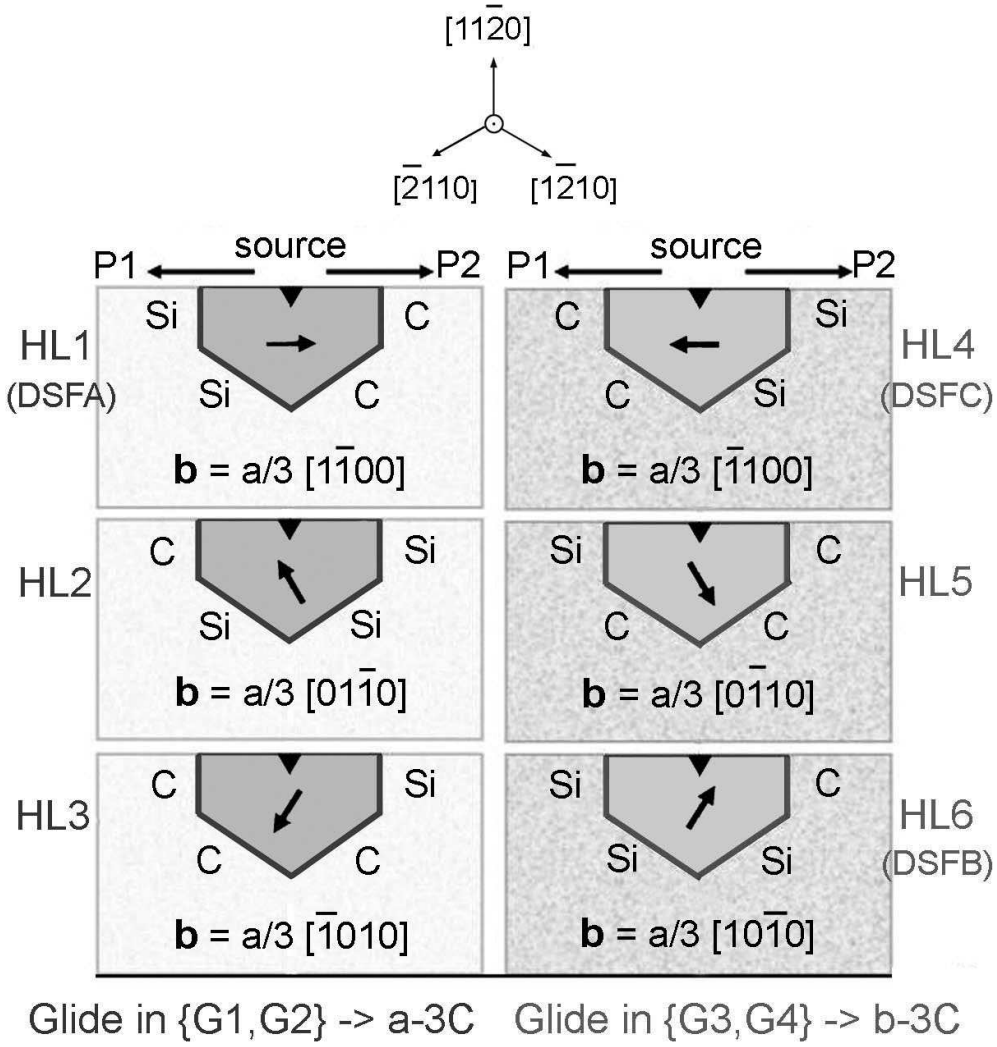

Lancin figure 7 grey
103x110mm (300 x 300 DPI)